Acta Materialia 297 (2025) 121294

Contents lists available at ScienceDirect

Acta Materialia

journal homepage: www.elsevier.com/locate/actamat

Full length article

Toward a universal framework for avalanche dynamics: From crystal slip to fault slip

Mostafa M. Omar *, Jaafar A. El-Awady

Department of Mechanical Engineering, Johns Hopkins University, 3400 N. Charles St., Baltimore, 21218, MD, USA

ARTICLE INFO

Keywords:
Dislocation avalanches
Acoustic emissions
Dislocation dynamics
Insitu microtesting

ABSTRACT

Sudden bursts of energy release, commonly referred to as "avalanches", are ubiquitous in many complex systems, from seismic activities in the Earth's crust to microscale dislocation activities in crystal lattices. Despite the massive differences in the underlying energy release mechanisms and their time and length scales, these events often display remarkable similarities, hinting at shared governing principles. In this study, we establish a direct analogy between dislocation avalanches in single-crystal nickel and seismic activity by combining *in situ* microcompression experiments with high-resolution acoustic emissions (AE) measurements. By correlating abrupt strain bursts with the spectral and temporal characteristics of AE signals, we introduce a new framework to identify "mainshock"-like events during dislocation avalanches and correlate them with their foreshocks and aftershocks. Our results show that the intermittent, scale-free dynamics of dislocation avalanches mirror earthquake statistics, including the Gutenberg–Richter, Omori, and Båth laws, providing phenomenological rules that describe energy release and event clustering in dislocation avalanches. This reflects the universality of these laws across widely different length and time scales and material systems. Additionally, while the overall avalanche statistics remain independent of the micropillar diameter, the magnitude of AE signals and load drops exhibits a strong size dependence. Overall, these findings increase our understanding of the fundamental mechanisms that govern plasticity and underscore the robust analogy between dislocation-mediated deformation and seismic processes.

1. Introduction

Many complex systems across different scientific domains often share fundamental scale-invariant behavior and governing principles despite operating under different physical mechanisms, driving forces, boundary conditions, and spatial/temporal scales. One manifestation of such universal features is the emergence of sudden, collective burst events that seemingly follow power-law or avalanche-like statistics. Examples range from Barkhausen noise in ferromagnets [1,2], neural avalanches in the brain [3], avalanches in granular flows [4], to plastic deformation in metals and seismic activity during earthquakes [5,6].

Among these examples, the parallels between plastic deformation in metals and seismic activities are particularly intriguing. In earthquakes, large-scale slip along faults in the Earth's crust abruptly releases energy, generating seismic waves that propagate through the subsurface [7,8]. Analogously, in crystalline metals, slip occurs via dislocations, which are line defects in the crystal that can slip collectively and suddenly, forming what are known as dislocation avalanches [9]. These avalanches release energy in the form of acoustic emissions (AE) as they move and interact through the crystal lattice, mirroring the seismic waves emitted during fault slip [10,11].

Remarkably, although dislocation avalanches and earthquakes differ by more than ten orders of magnitude in length and time scales, their statistical and scaling behaviors are strikingly similar [6,12]. Both phenomena exhibit scale-free statistics and self-organized criticality (SOC), implying that shared fundamental principles drive the dynamics of these distinct complex systems [5,10,11].

Despite these intriguing analogies, most dislocation avalanche studies have focused primarily on their statistical parallels with earthquakes [5–7,12–15], thus enriching our understanding of their common statistical mechanics. However, most studies have overlooked the detailed dynamics and underlying physics of individual dislocation avalanches. For instance, bulk-scale experiments average out many overlapping avalanches that may be spatially uncorrelated, while microscale experiments typically rely on load–displacement measurements that miss critical short-timescale features. As a result, neither method fully captures the onset, evolution, exhaustion, or mutual interactions of dislocation avalanches. This underscores the need for

* Corresponding author.
E-mail addresses: momar5@jhu.edu (M.M. Omar), jelawady@jhu.edu (J.A. El-Awady).

https://doi.org/10.1016/j.actamat.2025.121294
Received 28 February 2025; Received in revised form 29 May 2025; Accepted 25 June 2025
Available online 10 July 2025
1359-6454/© 2025 Acta Materialia Inc. Published by Elsevier Inc. All rights are reserved, including those for text and data mining, AI training, and similar technologies.

smaller-scale, higher-resolution AE investigations capable of isolating individual avalanche events and elucidating the correlation between mechanical responses and AE signals during microscale plastic deformation.

To address this, here, we perform *in situ* microcompression experiments with real-time AE measurements on single-crystal nickel micropillars. By analyzing the mechanical and acoustic responses of micropillars of varying sizes, we aim to resolve the high-resolution dynamics of dislocation avalanches in both the mechanical and frequency domains. This approach allows us to investigate how the size of the sample influences the intermittency and overlap of dislocation events, thus influencing the AE signals and the overall response to plastic deformation.

2. Materials and methods

2.1. Material and specimen fabrication

In this study, we use single-crystal high-purity nickel (Ni) acquired from Goodfellow Corporation, USA, with a purity level of 99.999%. The original Ni bar was cut using electrical discharge machining (EDM) into a cuboid with dimensions $3.3 \times 3.3 \times 9.0$ mm^3. Next, this cuboid was cut to align the top surface with the $[\bar{3}5\bar{2}]$ crystallographic orientation. Subsequently, the sample was mechanically polished, electropolished, and then heat treated as detailed in [16]. The micropillars were then fabricated on the top surface using the annular milling technique in a Thermo Scientific Helios G4 UC focused ion beam (FIB) system, operating at a voltage of 30 kV. More details of the fabrication can be found in [17].

Three different sizes of micropillars were fabricated with diameters of 5, 10, and 15 μm (referred to hereafter as D5, D10, and D15 micropillars, respectively), each with an aspect ratio of ≈ 2. The orientation of all micropillars was aligned along the $[\bar{3}5\bar{2}]$ crystallographic direction to allow for predominantly single-slip deformation. The Schmid factor for the primary slip system in this configuration is 0.45, while the next highest was 0.34.

2.2. Experimental setup

In situ uniaxial compression tests on the micropillars were carried out within a Tescan Mira3 scanning electron microscope (SEM). The SEM was equipped with a Nanomechanics InSEM cradle mounted on the SEM stage, which included an InForce 1000 actuator (1 *N* load cell). During testing, a conical diamond tip with a flat end (25 μm diameter) was used to interface with the micropillars. All tests were performed in a load-controlled manner with a loading rate of 0.16 mN/s and a data acquisition rate of 0.6 kHz.

A custom-designed fixture was used, as shown schematically in Fig. 1(a), to integrate the AE sensor with the InSEM cradle without obstructing either the field of view or the actuator tip path, while also ensuring consistent contact and positioning such that the sensor has a direct acoustic pathway from the sample. An SEM micrograph of the setup is shown in Fig. 1(b). All AE signals are recorded during the microcompression experiments with an acquisition rate of 2 MHz using a commercial PICO piezoelectric sensor, a 2/4/6 preamplifier (60 dB), and a PCI-2-based data acquisition system available from Physical Acoustic Corporation (MISTRAS).

2.3. Data analysis

2.3.1. AE waveforms processing

AE waveforms were recorded during the experiments and subsequently post-processed in MATLAB [18] to enhance their signal-to-noise ratio (SNR) by applying a bandpass filter (bandwidth = 30–50 kHz) to the raw waveforms. This bandwidth is based on spectral analysis of the waveforms that show that the signals associated with dislocation motion are most prominent in this range, whereas noise signals are largely removed, as discussed in Section 3.2.

The filtered AE waveforms are also segmented into "hits" using a hit definition time (HDT) of 100 μs and an amplitude threshold of 16 dB. Here, a hit is defined as the segment of the waveform that exceeds the specified amplitude threshold, with the hit ending when there is no further threshold crossing for a duration equal to the HDT. This approach is commonly used to separate genuine AE signals from background noise. Additional details of the conversion process can be found in our previous work [17].

3. Results and discussion

3.1. Mechanical and acoustic response

Representative stress–strain curves for the three micropillar sizes tested are shown in Fig. 2(a). The results show that the D5 micropillars exhibit a higher flow strength compared to the D10 micropillars, which, in turn, are higher than the D15 ones. This trend is consistent with the well-established size effects in metals—often referred to as "smaller is stronger"—and aligns with previous findings on many metallic systems (*cf.* [9,19–22]). In addition, all curves show characteristic intermittent behavior, where strain bursts become more pronounced as the diameter of the micropillar decreases.

Fig. 2(b) shows the recorded AE waveform for sample D5-2, showing a response representative of all other samples regardless of the micropillar size. The signal consists of high-amplitude bursts superimposed on a low-amplitude continuous background noise. The continuous noise, distinguished by its approximately constant amplitude, persists throughout the entire deformation and arises from the convolution of various sources, including the sensor, the wiring, and the acquisition board [23]. Importantly, each high-amplitude AE burst occurs exclusively with a displacement burst as shown in Fig. 2(c). These discrete events reflect the plastic deformation in the micropillars, which manifests itself as sudden displacement bursts accompanied by AE waves. In particular, at the onset of a displacement burst, the rate of energy release increases significantly, resulting in a pronounced increase in the AE amplitudes. Because the micropillars are single-crystals that are oriented for single-slip deformation, these AE bursts are mostly induced by dislocation avalanches on the active slip planes [17].

Fig. 2(d) shows the spectrogram of the AE waveform segment shown in (c). The spectral analysis reveals pronounced shifts in the frequency power distribution correlated with each displacement burst. Specifically, at the onset of the bursts, frequencies below 50 kHz dominate, leading to higher power within these bandwidths compared to other frequencies. It should be noted that, owing to the spectrogram's 1 ms time resolution, the corresponding frequency resolution is limited to 7.32 kHz. Therefore, the exact dominant frequency cannot be determined with higher precision from this plot.

Collectively, Figs. 2(c) and (d) demonstrate that the deformation events in the micropillars exhibit distinct signatures in both the time and frequency domains, namely, higher amplitude in the time domain and a comparatively narrow dominant bandwidth in the frequency domain. These observations underscore the need for a more in-depth analysis of the activities during the bursts. Fig. 3 shows a magnified excerpt of the spectrogram presented in Fig. 2(d), and it reveals intermittent activity even within a single displacement burst, which is characterized by discrete shifts in the frequency power distribution. In addition, while the dominant frequency range remains consistent, the corresponding power varies, as observed by the changes in the intensity of the red contours. This variation implies that the underlying AE source strength is not constant, highlighting an analogy between dislocation activities and seismic events, where individual earthquakes vary in magnitude within a single seismic sequence.

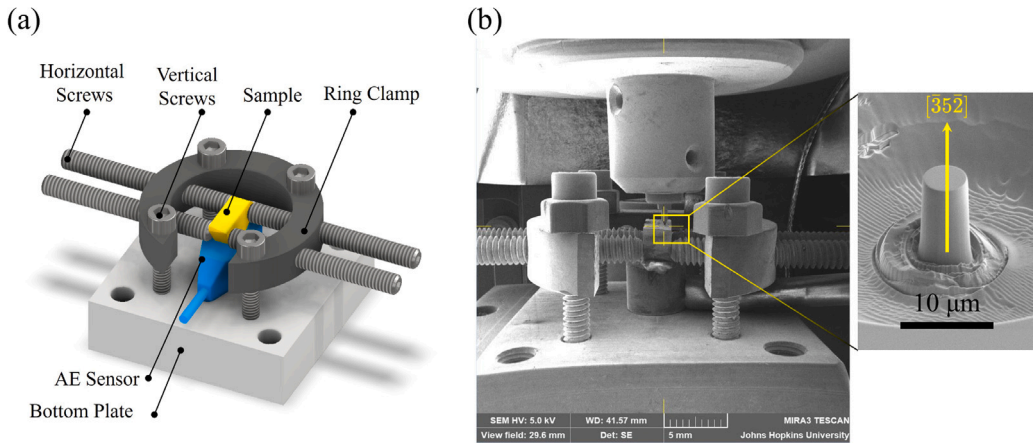

Fig. 1. (a) A 3D schematic of the custom-designed fixture used to couple the AE sensor with the sample in the InSEM cradle. (b) An SEM image of the experimental setup. The insert shows one of the micropillars fabricated into the surface before testing.

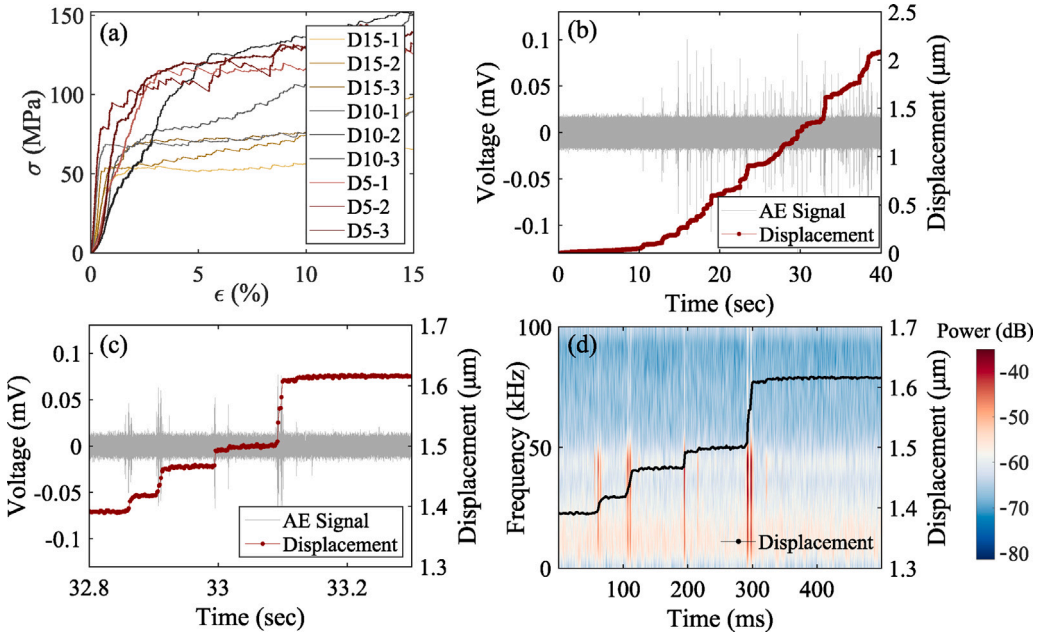

Fig. 2. The mechanical and acoustic response of the tested micropillars. (a) Representative stress–strain curves for the three micropillar sizes tested. (b) The AE waveform (measured as voltage versus time) overlaid on the displacement-time curve for D5-2 micropillar. (c) Enlarged view of a segment of the curves in (b), showing the synchronization between the displacement bursts and the AE bursts. (d) Plot of the spectrogram (power versus frequency and time) for the waveform segment in (c), with displacement plotted on the right *y*-axis. The spectrogram was generated using the "pspectrum" command in MATLAB with a time resolution of 1 ms. The *x*-axis is normalized to highlight the time scale of the events. (For interpretation of the references to color in this figure legend, the reader is referred to the web version of this article.)

3.2. From seismology to plasticity: A new physical perspective on foreshocks, mainshocks, and aftershocks during dislocation avalanches in metals

In seismology, earthquake sequences typically involve three main sequential events: foreshocks, mainshocks, and aftershocks. Foreshocks occur first, often because smaller localized slip patches activate on a fault nearing a critical stress threshold. These smaller events redistribute the stresses on neighboring regions, making the fault more susceptible to a larger rupture. Once friction resistance is overcome in a sufficiently large area, rupture can propagate dynamically, producing the mainshock, which is characterized by the release of the greatest seismic energy in that sequence of events [24]. After the mainshock, the damaged rock volume continues to rearrange under the newly altered stress field, giving rise to aftershocks. Over time, as the system gradually relaxes toward a new equilibrium, aftershocks diminish in frequency and eventually cease.

In metals, an analogous hierarchy of events can be identified in terms of dislocation avalanches. Similar to seismic activity, smaller bursts of dislocation motion, akin to foreshocks, can serve as precursors to larger avalanches by locally enhancing or redistributing stress within the crystal lattice. Once a critical stress state is reached in a specific region, a more substantial avalanche, or "mainshock", is triggered. Subsequently, additional smaller avalanches, akin to aftershocks, may occur as the material transitions toward a new equilibrium configuration.

Applying this earthquake-inspired analogy to dislocation avalanches, however, is not straightforward. In earthquakes, foreshocks and aftershocks occur within a zone surrounding the mainshock's epicenter—the ruptured fault segment. Events occurring outside this zone are generally considered independent earthquakes [25,26]. This spatial identification is feasible in seismology due to the deployment of numerous sensors capable of triangulating earthquake epicenters. On the other hand,

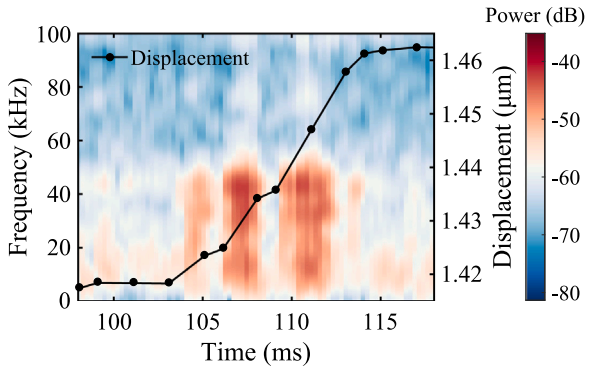

Fig. 3. A close-up view of the spectrogram in Fig. 2(d), showing discrete changes in the frequency power distributions during a single displacement burst event. (For interpretation of the references to color in this figure legend, the reader is referred to the web version of this article.)

dislocation avalanches involve a large number of active sites (dislocation sources) that can be near or far from one another, and the limited spatial resolution of AE sensors makes it challenging to spatially correlate different events. Nevertheless, the concept of foreshocks, mainshocks, and aftershocks still provides a valuable approach to study dislocation-mediated plasticity.

Previous approaches to define mainshocks in dislocation avalanches have often involved categorizing AE bursts by predefined energy thresholds [6,27,28]. In these approaches, AE events exceeding a certain energy range are designated as mainshocks, while lower-energy bursts situated between two mainshocks are classified as aftershocks. However, such methods face several limitations:

- The energy thresholds used are frequently arbitrary and may not correlate to any physical phenomena within the material.
- Events occurring between two mainshocks may ambiguously qualify as aftershocks of the first or foreshocks of the second, causing classification inconsistencies.
- If a substantial time gap separates two mainshocks, it becomes questionable to assume intervening events still belong to the earlier mainshock sequence.

To overcome these issues, we introduce a new definition of mainshocks in microscale plasticity, one that leverages the bursts observed in the stress–strain response and their associated AE signals. By examining the spectral characteristics of AE waveforms only within the discrete time intervals where bursts occur, we aim to capture the fundamental dislocation activity driving each burst independently, thereby providing a clearer analogy with seismic processes.

Fig. 4 shows a multi-dimensional analysis of rapid dislocation dynamics during a single displacement burst in the D15-2 micropillar as a representative example. In Fig. 4(a), a high-resolution excerpt of the raw AE waveform recorded during one of the identified displacement bursts is overlaid with the corresponding displacement-time curve. During the burst, the displacement jumps suddenly before the avalanche ceases. In Fig. 4(b), the time-dependent variation of the peak power across all frequencies of the AE waveform is shown for the same displacement burst. It shows that the incoming wave power changes notably during the displacement burst. Lastly, Fig. 4(c) shows the normalized power spectral density (PSD) of the waveform, highlighting that most of the power is concentrated in the range of 40 to 50 kHz bandwidth.

Two key insights emerge from this analysis. First, the peak frequency remains within a well-defined range throughout the deformation event, suggesting that the AE signals originate from similar or consistent sources. Second, the power of this peak frequency follows a rise-and-decay trend, analogous to the foreshock–mainshock–aftershock sequence in seismic events. This indicates a systematic evolution of dislocation activity during a displacement burst.

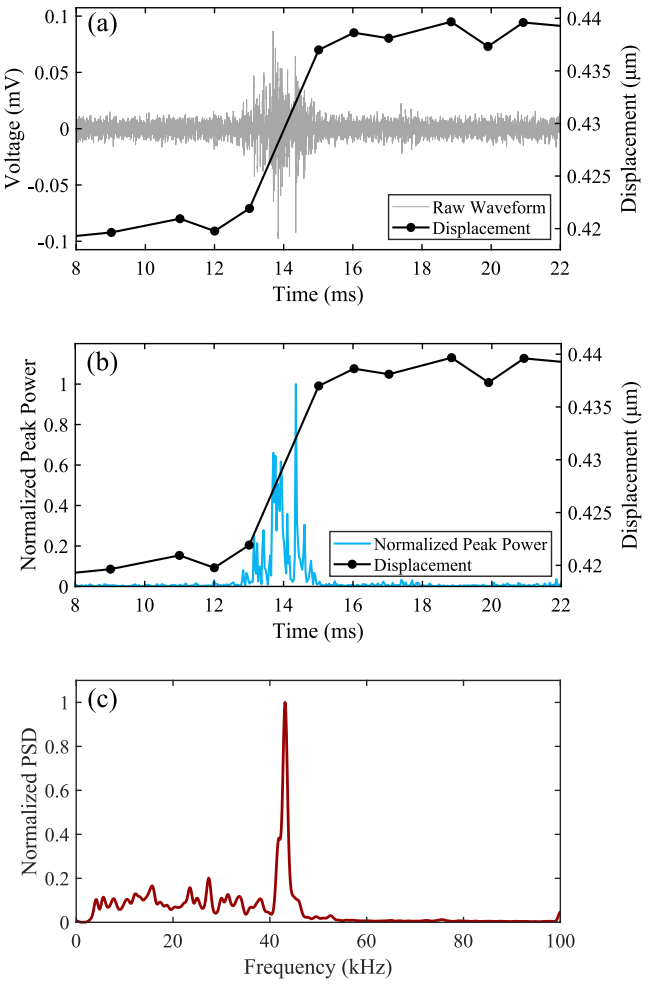

Fig. 4. Multi-dimensional analysis of rapid dislocation dynamics during a strain burst in the D15-2 micropillar. (a) Temporal evolution of the raw AE waveform (left axis) superimposed with the corresponding displacement-time curve (right axis) during a single displacement burst. (b) Time-dependent variation of the peak power across all frequencies. The *y*-axis is normalized with respect to the maximum value. (c) Normalized power spectral density (PSD) of the waveform shown in (a), highlighting a dominant bandwidth of 40–50 kHz.

Accordingly, we introduce a new methodology for studying foreshock and aftershock behavior in microscale plasticity by correlating AE events with displacement bursts. Specifically, only AE bursts occurring within the same displacement burst interval are considered correlated, as illustrated in Fig. 5(a). In this approach, the filtered waveform during every displacement burst is subdivided into small wavelet packets, as schematically shown in Fig. 5(b). Each packet begins when the AE amplitude exceeds the prescribed threshold and ends when the amplitude falls below it.

To classify these packets, we first compute their amplitude and energy. Secondly, the packet with the highest amplitude within a burst is designated as the mainshock. All packets preceding the mainshock are classified as foreshocks, and those following it are classified as aftershocks. This approach allows for a more physically grounded analysis of dislocation dynamics, enabling us to draw more meaningful parallels with seismic events.

One potential concern with this definition is that the lower-amplitude packets following the mainshock might result from wave reflections off the sample sidewalls. To investigate this possibility, we calculated the reflection time for both shear and longitudinal waves to traverse the longest substrate dimension (6.6 mm). Given that the shear wave velocity in Ni is approximately 3000 m/s [29], a shear

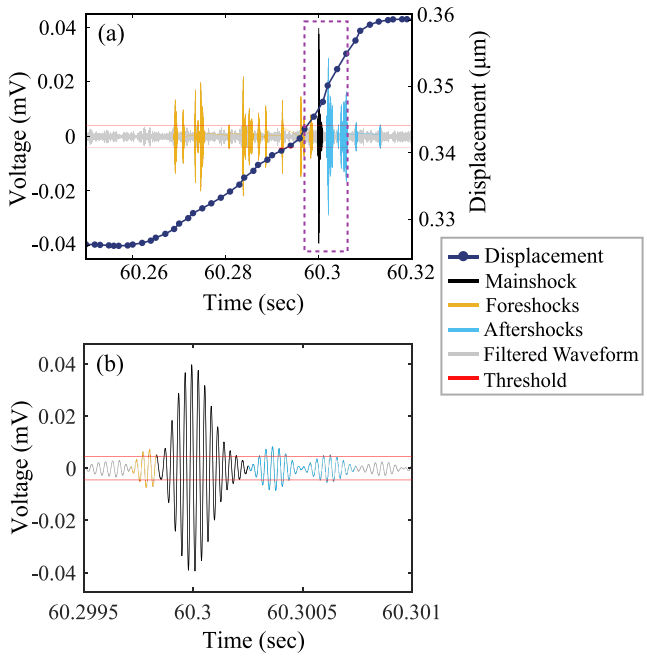

Fig. 5. Schematic for identification of foreshocks, mainshocks, and aftershocks from AE measurements during each displacement burst. (a) An excerpt from a representative filtered AE waveform corresponding to a single burst event, illustrating the classification of foreshocks (yellow lines), mainshock (black line), and aftershocks (light blue lines). (b) Enlarged view of the dash-box in (a), showing how each wavelet packet begins when the AE amplitude exceeds a predefined threshold and ends when it falls below it. This approach allows for the differentiation of individual events within the same burst. (For interpretation of the references to color in this figure legend, the reader is referred to the web version of this article.)

wave would reflect from one side to another in about ≈ 2.2 μsec, and for longitudinal waves, with a velocity of ≈ 6040 m/s [29], the reflection time is even shorter. However, the actual waiting times between foreshocks, mainshocks, and aftershocks are on the order of milliseconds, which is three orders of magnitude longer than the calculated reflection times. This substantial time difference confirms that the observed foreshocks, mainshocks, and aftershocks are not simply reflections of an AE event from the sample sidewalls. Instead, they represent distinct dislocation events triggered by sequential stress redistribution during displacement bursts.

3.2.1. Energy scaling and correlations among mainshocks, foreshocks, and aftershocks in dislocation avalanches

In this section, we analyze the correlations between the foreshock, mainshock, and aftershock energies during dislocation avalanches to gain insights into the nature of energy release during deformation and quantify their parallels with seismic phenomena.

Fig. 6 shows the correlations between each mainshock energy and its corresponding foreshocks/aftershocks energies. Data points are colored according to the strain value the displacement bursts occur at. In Figs. 6(a) and 6(c), we plot the energies of each foreshock or aftershock, respectively, against the energy of its associated mainshock. Although scattered, a positive correlation is evident: more energetic mainshocks tend to be associated with more energetic foreshocks and aftershocks. This suggests that high-energy dislocation activities tend to cluster in time. Moreover, most of the high-energy mainshocks occur at lower strains (bluish data points), while at higher strain values, less energetic mainshocks predominantly occur (reddish data points). This observation is consistent with our previously reported strain-dependent AE energy trend (see [17]).

Figs. 6(b) and 6(d) show the same data, but by plotting the average foreshock and aftershock energies associated with a single mainshock, respectively, against the associated mainshock energy. The observed trends reinforce the positive correlations, implying a hierarchical process of energy release during a dislocation avalanche. Because the actuator continues to impose displacement during a burst, the resolved shear stress on the active slip plane does not relax after the largest packet. Symmetric loading conditions, therefore, would favor comparable foreshock and aftershock energies, in contrast to earthquake faults, where the mainshock releases most of the accumulated stress.

3.3. A comparative analysis of seismic statistical models applicability to dislocation avalanches

In this section, we examine further parallels between seismic activities and dislocation avalanches by examining the universality of seismic scaling laws against our AE measurements during dislocation avalanches. In seismology, correlations in energy release between foreshocks, mainshocks, and aftershocks are key to understanding earthquake clustering and making predictions of the next event. Analogously, applying the same approach to dislocation avalanches could enhance our ability to predict slip localization.

3.3.1. The mainshock magnitude-frequency relationship

The Gutenberg–Richter (GR) law is a cornerstone in seismology for describing the frequency–magnitude distribution of earthquakes. It states that the number of earthquakes, N, with a magnitude greater than or equal to M follows an exponential relationship:

$$log_{10} N = a - bM \tag{1}$$

where a and b are constants [30,31]. This implies that smaller earthquakes occur much more frequently than larger ones.

We apply this concept to dislocation avalanches by considering the AE energy associated with a burst as analogous to the earthquake magnitude. If the AE energy follows the GR law, we expect a power-law distribution. Fig. 7(a) shows the probability density function (PDF) of the AE mainshock energies for all tested micropillars. The data clearly exhibit a power-law behavior spanning more than three orders of magnitude, following the form:

$$P(E_{MS}) \propto E_{MS}^{-\alpha} \tag{2}$$

where $P(E_{MS})$ is the probability density (calculated as described in Supporting Information Section 2), E_{MS} is the AE mainshock energy, and α is the power-law exponent. Our analysis yields $\alpha = 1.60$, which is remarkably close to the exponent of 1.66 observed in earthquakes [6,31,32]. This striking similarity suggests that the processes governing energy release in dislocation avalanches and earthquakes are fundamentally analogous.

3.3.2. Temporal decay of aftershocks rates

Omori's law describes the decay of aftershocks frequency following a mainshock, and is expressed as:

$$\dot{N}(t) \propto t^{-p} \tag{3}$$

where $\dot{N}(t)$ is the rate of aftershocks at time t after the mainshock event, and p is the decay exponent, which typically ranges from 0.9 to 1.5 for earthquakes [33,34].

Fig. 7(b) shows how the aftershock rate declines over time for each mainshock in our experiments. The data closely follow a power-law decay with an exponent of 1 across three orders of magnitude in time, which is consistent with Omori's law (Eq. (3)). This indicates that aftershocks in dislocation avalanches decay in a manner analogous to seismic aftershocks.

However, at longer time scales ($t > 0.04$ sec), the decay is steeper ($p \approx 3.1$), deviating from the classical Omori exponent. This steeper decay indicates a shift in the dominant mechanisms governing aftershock events at longer time scales within the active dislocation system.

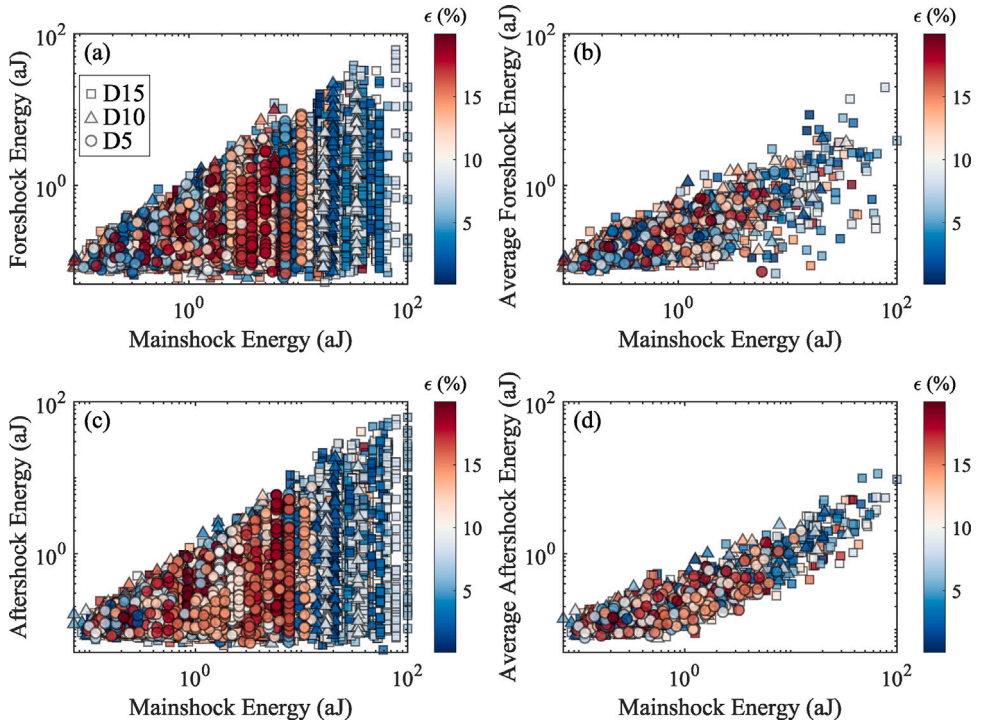

Fig. 6. Energy correlations between mainshocks and their associated foreshocks and aftershocks, with data points colored by the strain level the burst occurs at. (a) Scatter plot of individual foreshock energies versus their associated mainshock energies. (b) Average foreshock energy associated with a single mainshock versus the associated mainshock energy. (c) Scatter plot of individual aftershock energies versus their associated mainshock energies. (d) Average aftershock energy associated with a single mainshock versus their associated mainshock energy. (For interpretation of the references to color in this figure legend, the reader is referred to the web version of this article.)

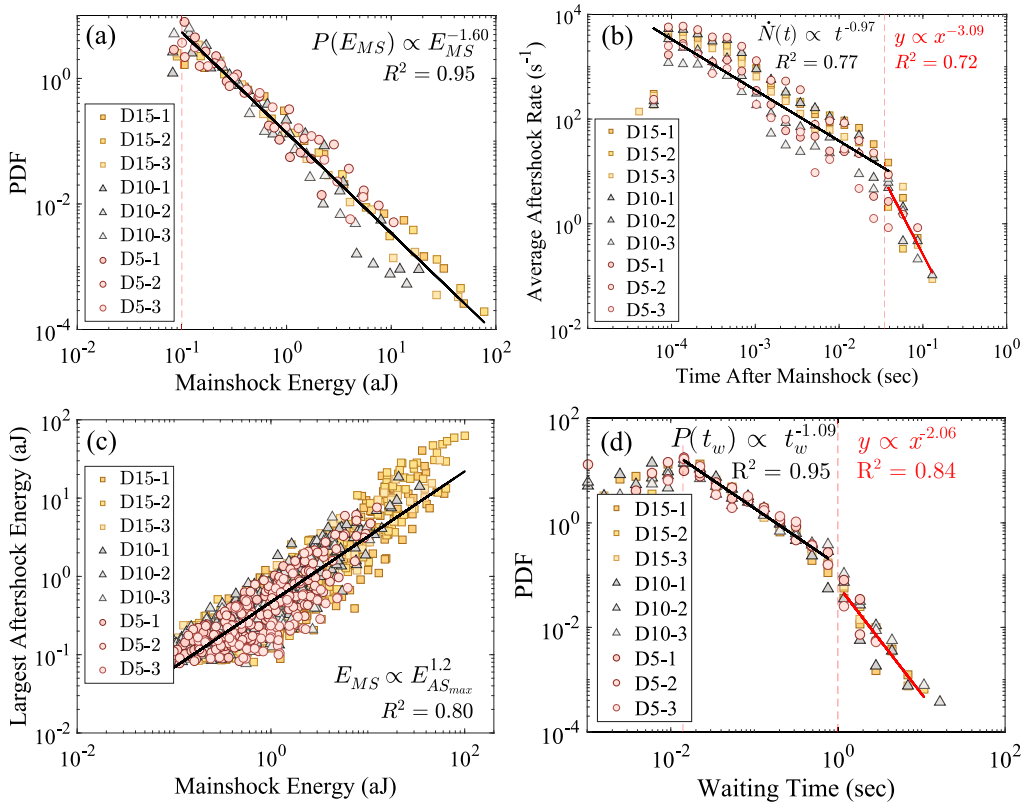

Fig. 7. Statistical behavior of the shocks. (a) Probability density distribution of mainshock energies (E_{MS}) in dislocation avalanches. The data follow a power-law distribution similar to Eq. (2) with an exponent $\alpha = 1.60$, closely matching the Gutenberg–Richter law for earthquakes. (b) Temporal decay of aftershock rates following mainshocks in all tested micropillars. (c) Correlation between mainshock energies (E_{MS}) and their largest aftershock energies ($E_{AS_{max}}$) for all tested micropillars. (d) Probability density distribution of the waiting times (t_w) between dislocation bursts for all tested micropillars.

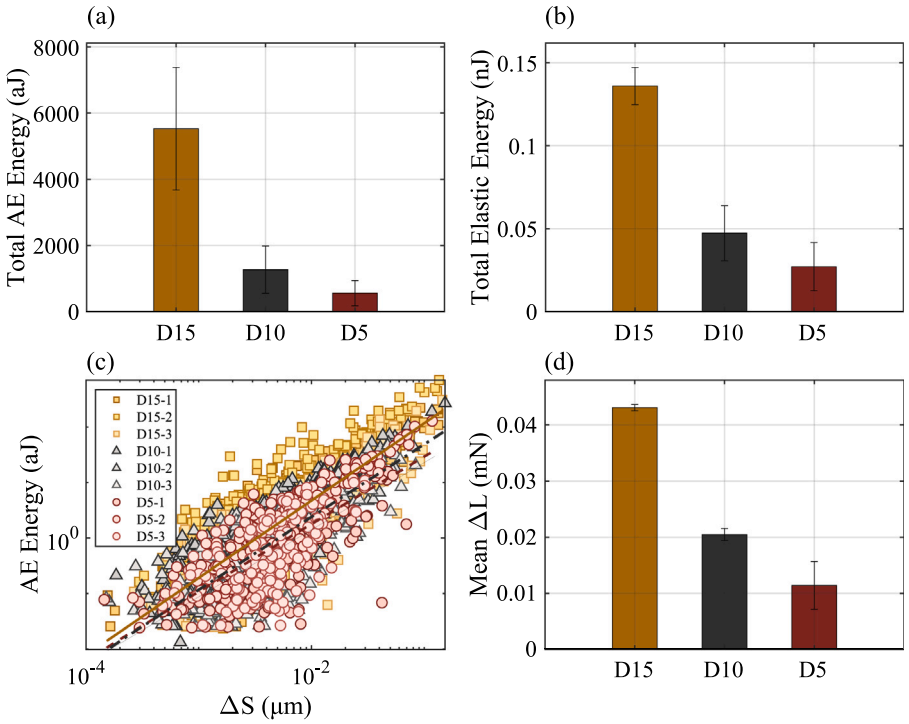

Fig. 8. Size effects on the acoustic and mechanical response. (a) Total measured AE energy for different micropillar sizes. (b) Total released elastic energy, calculated from the load–displacement curves, as a function of micropillar sizes. (c) Correlation between displacement burst magnitude (ΔS) and the corresponding AE energy measured during the burst. The straight lines show best fits to a power-law form $E_{AE} \propto \Delta S^{\gamma}$. The colors represent the micropillar size. The red (dashed), black (dash-dotted), and orange (solid) lines with $\gamma = 1.13$ and $R^2 = 0.55$, $\gamma = 1.15$ and $R^2 = 0.61$, and $\gamma = 1.27$ and $R^2 = 0.66$ represent fits for the D5, D10, and D15 micropillars, respectively. (d) Mean load-drop magnitude (ΔL) during bursts for different micropillar sizes, showing a decrease with decreasing micropillar diameter. (For interpretation of the references to color in this figure legend, the reader is referred to the web version of this article.)

3.3.3. Ratio of mainshock energy to largest aftershock energy

Båth's law in seismology states that the difference in magnitude between a mainshock and its largest aftershock is approximately constant, typically around 1.1–1.2 [32]. This reflects a consistent scaling in the energy partitioning between mainshocks and their largest aftershocks.

We examine this relationship by plotting the logarithm of the mainshock energies against that of the largest aftershock energies, as shown in Fig. 7(c). The data is observed to follow a linear relationship with a slope of 1.2, aligning with Båth's Law.

3.3.4. Waiting time statistics between dislocation avalanches

The distribution of waiting time between dislocation avalanches provides insights into the temporal clustering and correlation of plastic deformation events. In seismology, waiting times between earthquakes exceeding a certain energy threshold are observed to follow a power-law distribution [32].

A similar phenomenon is also observed in our data on dislocation avalanches. Fig. 7(d) shows the probability density distribution of waiting times (t_w) between bursts. The distribution follows a power-law relationship of the form:

$$P(t_w) \propto t_w^{-\beta} \tag{4}$$

with $\beta \approx 1.09$ over two orders of magnitude in time. This exponent agrees closely with previously reported values for dislocation plasticity and also aligns with corresponding measurements in earthquakes [6]. The power-law behavior indicates a substantial temporal correlation among dislocation bursts, suggesting that once one event occurs, subsequent events are more likely within a certain time frame.

At longer waiting times, however, a deviation from the power-law behavior is observed, with a steeper decay rate ($\beta \approx 2.06$). This deviation may be attributed to changes in the internal stress state of the material or the exhaustion of readily available dislocation sources over extended periods. Such changes can reduce the probability of subsequent events, leading to a steeper decline in the waiting time distribution.

3.4. Size-dependent acoustic emission behavior

Fig. 7 demonstrates that the statistical behavior of the displacement bursts is nearly size-independent, as no clear differences emerge among micropillars of different sizes. This suggests that the underlying dislocation avalanche dynamics are similar across the micropillar sizes tested here. However, a more detailed analysis of the acoustic signals reveals a significant dependence on micropillar size.

Fig. 8(a) shows that the total measured AE energy decreases as the micropillar diameter decreases, even though smaller micropillars exhibit higher flow strengths (see Fig. 2(a)). This observation indicates that the micropillar's strength is not the primary factor determining the strength of its acoustic response.

Further evidence for this size effect is shown in Fig. 8(b), which shows the total released elastic energy (calculated from the load–displacement curves) for different micropillar sizes. A similar decreasing trend with decreasing diameter is observed, indicating that larger micropillars release more elastic energy during strain bursts.

Moreover, Fig. 8(c) shows the correlation between displacement-burst magnitude, ΔS, and the associated AE energy. Despite considerable scatter in the data, a positive correlation is observed, with slightly higher exponents for larger micropillars. This suggests that larger displacement bursts, which are – on average – more prevalent in larger micropillars (see Fig. S1), generate stronger AE signals, likely

due to the higher number of available dislocation sources and more extensive dislocation dynamics.

As shown in Fig. 8(d), the mean load-drop magnitude decreases with decreasing sample diameter, mirroring the trend observed in AE energy. The D15 micropillars exhibit higher mean load drops, indicating that the "source strength" (i.e., the magnitude of dislocation activities) is greater in larger micropillars even though the mean stress-drop size shows an inverse trend, as shown in Fig. S2. Collectively, these observations indicate a direct correlation between AE energy and micropillar size, reflecting how the micropillar size influences the mechanical response and the energy-release mechanisms during plastic deformation.

In summary, while the statistical analyses of the bursts show size independence, suggesting similar avalanche dynamics across length scales from micrometers to kilometers, both the AE and mechanical response show significant size-dependent effects. Specifically, larger micropillars generate stronger AE signals and exhibit larger load drops, which can be attributed to the increase in dislocation numbers and activity. These findings highlight the importance of considering sample size when interpreting AE responses during dislocation avalanche behaviors in materials.

4. Conclusion

This study bridges the gap between dislocation plasticity and seismic phenomenon by integrating *in situ* microcompression experiments with acoustic emissions (AE) measurements, thus drawing insightful parallels between dislocation avalanches in metals and earthquake events. By redefining mainshocks based on the bursts observed in stress–strain curves, we proposed a new approach that correlates AE signals with distinct avalanche events, offering clearer insights into the onset, evolution, and interactions of dislocation avalanches at the microscale. Through detailed waveform analysis and the identification of high-energy wavelet packets, we distinguished mainshocks from their associated foreshocks and aftershocks, revealing a cascading pattern of plastic deformation. This perspective goes beyond traditional stress–strain analyses by highlighting the temporal correlations inherent in dislocation dynamics.

Our results also show a complex relationship between micropillar size and its mechanical and acoustic responses. Although larger micropillars exhibited stronger acoustic emissions, demonstrated by higher AE energies and larger load drops, the underlying behavior driving acoustic emissions and dislocation activity were analogous across different scales. We further demonstrate that the energy relationships among foreshocks, mainshocks, and aftershocks exhibit scaling behaviors similar to those in seismic events, with power-law distributions conforming to established earthquake laws, including the Gutenberg–Richter and Omori laws. Nevertheless, deviations at longer time scales suggest shifts in the mechanisms driving aftershock activity, indicating a need for further investigation.

These findings underscore the universality of avalanche dynamics across disparate scales and systems. By showing that dislocation avalanches follow similar statistical laws to seismic phenomena, even sharing consistent energy ratios of mainshocks to their largest aftershocks, this work improves our understanding of microscale plasticity and opens up opportunities for further cross-disciplinary research in materials science and geophysics. Finally, recognizing the universal patterns in energy release and event correlations in avalanches can enhance our predictive models of material deformation and inform strategies to predict fracture and mitigate failure in engineering applications.

CRediT authorship contribution statement

Mostafa M. Omar: Writing – review & editing, Writing – original draft, Visualization, Methodology, Investigation, Formal analysis, Data curation, Conceptualization. **Jaafar A. El-Awady:** Writing – review & editing, Writing – original draft, Supervision, Project administration, Methodology, Funding acquisition, Conceptualization.

Funding sources

This research was sponsored by the National Science Foundation (NSF) under Grant No. 2225675.

Declaration of competing interest

The authors declare no competing interests.

Acknowledgments

The authors would like to express their gratitude to Dr. Steven Lavestein for helping with the design of the experimental setup and Dr. Ahmed Barakat for fruitful discussions.

Appendix A. Supplementary data

Supplementary material related to this article can be found online at https://doi.org/10.1016/j.actamat.2025.121294.

Data availability

Data will be made available on request.

References

[1] G. Durin, S. Zapperi, Scaling exponents for Barkhausen avalanches in polycrystalline and amorphous ferromagnets, Phys. Rev. Lett. 84 (20) (2000) 4705, http://dx.doi.org/10.1103/PhysRevLett.84.4705, https://journals.aps.org/prl/abstract/10.1103/PhysRevLett.84.4705.

[2] G. Durin, S. Zapperi, The Barkhausen effect, 2004.

[3] J.M. Beggs, D. Plenz, Neuronal avalanches in neocortical circuits, J. Neurosci. 23 (35) (2003) 11167–11177, http://dx.doi.org/10.1523/JNEUROSCI.23-35-11167.2003, https://www.jneurosci.org/content/23/35/11167 . https://www.jneurosci.org/content/23/35/11167.abstract.

[4] K.A. Dahmen, Y. Ben-Zion, J.T. Uhl, A simple analytic theory for the statistics of avalanches in sheared granular materials, Nat. Phys. 7 (7) (2011) 554–557, http://dx.doi.org/10.1038/nphys1957.

[5] S. Papanikolaou, D.M. Dimiduk, W. Choi, J.P. Sethna, M.D. Uchic, C.F. Woodward, S. Zapperi, Quasi-periodic events in crystal plasticity and the self-organized avalanche oscillator, Nature 490 (7421) (2012) http://dx.doi.org/10.1038/nature11568.

[6] P.D. Ispánovity, D. Ugi, G. Péterffy, M. Knapek, S. Kalácska, D. Tüzes, Z. Dankházi, K. Máthis, F. Chmelík, I. Groma, Dislocation avalanches are like earthquakes on the micron scale, Nat. Commun. 13 (1) (2022) 1975, http://dx.doi.org/10.1038/s41467-022-29044-7, https://www.nature.com/articles/s41467-022-29044-7. http://arxiv.org/abs/2107.13334.

[7] J. Baró, A. Corral, X. Illa, A. Planes, E.K.H. Salje, W. Schranz, D.E. Soto-Parra, E. Vives, Statistical similarity between the compression of a porous material and earthquakes, Phys. Rev. Lett. 110 (8) (2013) http://dx.doi.org/10.1103/PhysRevLett.110.088702.

[8] D.P. Hill, F.G. Fischer, K.M. Lahr, J.M. Coakley, Earthquake sounds generated by body-wave ground motion, Bull. Seismol. Soc. Am. 66 (4) (1976) 1159–1172, http://dx.doi.org/10.1785/BSSA0660041159, http://www.bssaonline.org/content/66/4/1159.short.

[9] M.D. Uchic, P.A. Shade, D.M. Dimiduk, Plasticity of micrometer-scale single crystals in compression, Annu. Rev. Mater. Res. 39 (1) (2009) 361–386, http://dx.doi.org/10.1146/annurev-matsci-082908-145422.

[10] M. Baiesi, M. Paczuski, Scale-free networks of earthquakes and aftershocks, Phys. Rev. E Stat. Phys. Plasmas, Fluids, Relat. Interdiscip. Top. 69 (6) (2004) 8, http://dx.doi.org/10.1103/PhysRevE.69.066106, http://www.scecdc.scec.org/ftp/.

[11] D.M. Dimiduk, C. Woodward, R. LeSar, M.D. Uchic, Scale-free intermittent flow in crystal plasticity, Science 312 (5777) (2006) 1188–1190, http://dx.doi.org/10.1126/science.1123889, http://www.ncbi.nlm.nih.gov/pubmed/16728635.

[12] J.T. Uhl, S. Pathak, D. Schorlemmer, X. Liu, R. Swindeman, B.A. Brinkman, M. LeBlanc, G. Tsekenis, N. Friedman, R. Behringer, D. Denisov, P. Schall, X. Gu, W.J. Wright, T. Hufnagel, A. Jennings, J.R. Greer, P.K. Liaw, T. Becker, G. Dresen, K.A. Dahmen, Universal quake statistics: From compressed nanocrystals to earthquakes, Sci. Rep. 5 (11) (2015) http://dx.doi.org/10.1038/srep16493.

[13] F. Meng, L.N.Y. Wong, H. Zhou, Power law relations in earthquakes from microscopic to macroscopic scales, Sci. Rep. 9 (1) (2019) 1–11, http://dx.doi.org/10.1038/s41598-019-46864-8, https://www.nature.com/articles/s41598-019-46864-8.

[14] J. Barés, A. Dubois, L. Hattali, D. Dalmas, D. Bonamy, Aftershock sequences and seismic-like organization of acoustic events produced by a single propagating crack, Nat. Commun. 9 (1) (2018) http://dx.doi.org/10.1038/s41467-018-03559-4.

[15] D. Houdoux, A. Amon, D. Marsan, J. Weiss, J. Crassous, Micro-slips in an experimental granular shear band replicate the spatiotemporal characteristics of natural earthquakes, Commun. Earth Environ. 2 (1) (2021) 1–11, http://dx.doi.org/10.1038/s43247-021-00147-1, https://www.nature.com/articles/s43247-021-00147-1.

[16] J.A. El-Awady, M.D. Uchic, P.A. Shade, S.L. Kim, S.I. Rao, D.M. Dimiduk, C. Woodward, Pre-straining effects on the power-law scaling of size-dependent strengthening in Ni single crystals, Scr. Mater. 68 (3–4) (2013) 207–210, http://dx.doi.org/10.1016/j.scriptamat.2012.10.035.

[17] M.M. Omar, J.A. El-Awady, Acoustic profiling of intermittent plasticity, Acta Mater. 285 (2025) 120646, http://dx.doi.org/10.1016/j.actamat.2024.120646.

[18] T.M. Inc., MATLAB version: 24.1.0.2603908 (R2024a), 2024, https://www.mathworks.com.

[19] M.D. Uchic, D.M. Dimiduk, J.N. Florando, W.D. Nix, Sample dimensions influence strength and crystal plasticity, Science 305 (5686) (2004) 986–989, http://dx.doi.org/10.1126/science.1098993, http://www.ncbi.nlm.nih.gov/pubmed/15310897. https://www.science.org/doi/10.1126/science.1098993.

[20] D.M. Dimiduk, M.D. Uchic, T.A. Parthasarathy, Size-affected single-slip behavior of pure nickel microcrystals, Acta Mater. 53 (15) (2005) 4065–4077, http://dx.doi.org/10.1016/j.actamat.2005.05.023, https://www.sciencedirect.com/science/article/pii/S1359645405002880#fig1.

[21] J.A. El-Awady, Unravelling the physics of size-dependent dislocation-mediated plasticity, Nat. Commun. 6 (2015) http://dx.doi.org/10.1038/ncomms6926, www.nature.com/naturecommunications.

[22] O. Kraft, P.A. Gruber, R. Mönig, D. Weygand, Plasticity in confined dimensions, Annu. Rev. Mater. Res. 40 (1) (2010) 293–317, http://dx.doi.org/10.1146/annurev-matsci-082908-145409.

[23] C.B. Scruby, An introduction to acoustic emission, J. Phys. E: Sci. Instrum. 20 (8) (1987) 946–953, http://dx.doi.org/10.1088/0022-3735/20/8/001, https://iopscience.iop.org/article/10.1088/0022-3735/20/8/001.

[24] K.R. Felzer, R.E. Abercrombie, G. Ekström, A common origin for aftershocks, foreshocks, and multiplets, Bull. Seismol. Soc. Am. 94 (1) (2004) 88–98, http://dx.doi.org/10.1785/0120030069, http://pubs.geoscienceworld.org/ssa/bssa/article-pdf/94/1/88/2717804/88_ssa03069.pdf.

[25] M. Liu, S. Stein, Earthquake, aftershocks, in: H.K. Gupta (Ed.), Encyclopedia of Solid Earth Geophysics, Springer International Publishing, Cham, 2019, pp. 1–4, http://dx.doi.org/10.1007/978-3-030-10475-7_204-1.

[26] L. Knopoff, Y.Y. Kagan, R. Knopoff, Beta Values for Foreshocks and Aftershocks in Real and Simulated Earthquake Sequences, vol. 10, 1982, http://dx.doi.org/10.1785/bssa0720051663.

[27] T. Mäkinen, A. Miksic, M. Ovaska, M.J. Alava, Avalanches in wood compression, Phys. Rev. Lett. 115 (5) (2015) 055501, http://dx.doi.org/10.1103/PhysRevLett.115.055501, https://journals.aps.org/prl/abstract/10.1103/PhysRevLett.115.055501.

[28] Z. Wang, J. Wang, J. Ayarza, T. Steeves, Z. Hu, S. Manna, A.P. Esser-Kahn, Bio-inspired mechanically adaptive materials through vibration-induced crosslinking, Nat. Mater. 20 (6) (2021) 869–874, http://dx.doi.org/10.1038/s41563-021-00932-5, https://www.nature.com/articles/s41563-021-00932-5.

[29] W.M. Haynes (Ed.), CRC Handbook of Chemistry and Physics, 95th ed., CRC Press, Boca Raton, FL, 2014, http://dx.doi.org/10.1201/b17118, https://www.taylorfrancis.com/books/9781482208689.

[30] B. Gutenberg, C.F. Richter, Magnitude and energy of earthquakes, Ann. Geophys. 9 (1) (1956) 1–15, http://dx.doi.org/10.4401/ag-5590.

[31] T. Utsu, Representation and analysis of the earthquake size distribution: A historical review and some new approaches, Pure Appl. Geophys. 155 (2–4) (1999) 509–535, http://dx.doi.org/10.1007/s000240050276, https://link.springer.com/article/10.1007/s000240050276.

[32] H.V. Ribeiro, L.S. Costa, L.G. Alves, P.A. Santoro, S. Picoli, E.K. Lenzi, R.S. Mendes, Analogies between the cracking noise of ethanol-dampened charcoal and earthquakes, Phys. Rev. Lett. 115 (2) (2015) 025503, http://dx.doi.org/10.1103/PhysRevLett.115.025503, https://journals.aps.org/prl/abstract/10.1103/PhysRevLett.

[33] F. Omori, On the after-shocks of earthquakes, J. Coll. Sci. Imp. Univ. Tokyo 7 (1894) 111–200.

[34] T. Utsu, Y. Ogata, The centenary of the omori formula for a decay law of aftershock activity, J. Phys. Earth 43 (1) (1995) 1–33, http://dx.doi.org/10.4294/jpe1952.43.1.